Journal of Power Sources 271 (2014) 312–325

Contents lists available at ScienceDirect

Journal of Power Sources

journal homepage: www.elsevier.com/locate/jpowsour

Mechanical exfoliation of graphite in 1-butyl-3-methylimidazolium hexafluorophosphate (BMIM-PF_6) providing graphene nanoplatelets that exhibit enhanced electrocatalysis

William Ignatius Hayes [a, *], Gennady Lubarsky [a], Meixian Li [b], Pagona Papakonstantinou [a]

[a] Engineering Department, University of Ulster at Jordanstown, Shore Road, Newtownabbey BT370QB, Northern Ireland, UK
[b] Department of Analytical Chemistry, Peiking University, 202 Chengfu Road, Haidian District, Beijing 100871, PR China

HIGHLIGHTS

- Reported is graphene nanoplatelets delivered by grinding graphite in BMIM-PF_6.
- Contrasted is structure, composition and ORR after varied grinding durations.
- Grinding decreases the nanoplatelet size, while increasing surface defects.
- Prolonging the graphite grinding before pyrolysis increases nitrogen incorporation.
- ORR catalysis is enhanced by prolonged grinding, with higher stability than Pt/C.

GRAPHICAL ABSTRACT

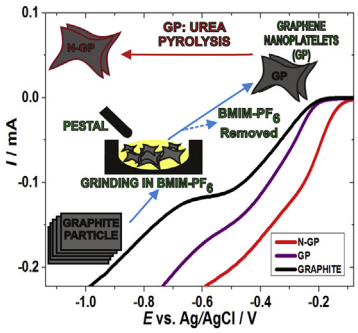

ARTICLE INFO

Article history:
Received 20 February 2014
Received in revised form
9 June 2014
Accepted 25 June 2014
Available online 14 July 2014

Keywords:
Nitrogen-doped graphene nanoplatelets
Grinding
Pyrolysis
Electrocatalysis
Oxygen reduction reaction
1-Butyl-3-methylimidazolium hexafluorophosphate

ABSTRACT

A novel production method for graphene nanoplatelets (GPs) with enhanced electrocatalytic behaviour is presented. GPs show improvement in their oxygen reduction reaction (ORR) catalysis after prolonging the grinding of graphite in 1-butyl-3-methylimidazolium hexafluorophosphate (BMIM-PF_6). Nitrogen doping of the GPs has inferred a further increase in ORR. The ORR onset potential, cathodic current magnitude and electron transfer efficiency have all improved as a direct consequence of increasing the graphite grinding duration from 30 min to 4 h. Atomic force microscopy has confirmed a decrease in the GP diameter and height as the grinding increases. Raman spectroscopy indicates a higher level of defects present after prolonging the graphite grinding in BMIM-PF_6, most likely a result of the increased edge plane exposure. This increased edge plane appears to promote a higher level of nitrogen incorporation as the graphite grinding duration increases, as confirmed by X-ray photoelectron spectroscopy analysis. The stability of the cathodic current assessed by chronoamperometry analysis is higher for the GP and nitrogen doped graphene nanoplatelet (N-GP) samples than the platinum on carbon black (Pt/C). This study presents a novel process for the production of nitrogen doped graphene nanoplatelets, constituting a strategy for the up-scaled production of electrocatalysts.

1. Introduction

To counter the issue of low availability and high expense, substitution of platinum-based electrocatalysts for cheaper and more

* Corresponding author. Tel.: +353 (0) 877155823.
E-mail address: Liamhayes6@hotmail.com (W.I. Hayes).

http://dx.doi.org/10.1016/j.jpowsour.2014.06.168
0378-7753/

abundant alternatives is continuously being sought [1,2]. Graphene has presented as one of the most promising avenues for the mass production of an electrode coating for fuel cell catalysis [3–5]. Graphenic materials are favourable when a high surface area, high conductivity, high strength and low cost material is required [6]. Notably, nitrogen doping assists in providing graphenic material that can deliver a similar or improved performance to that of platinum-derived catalysts [7–10].

Periodic density functional theory (DFT) calculations have suggested that the N-graphene edges and the N-dopant sites in the proximity of the edges are active catalytic sites for oxygen reduction [11]. The exact reaction mechanism of ORR catalysis at the surface of N-graphene has not yet reached a consensus. The adsorption of oxygen is noted to be a pivotal step in the initiation of ORR catalysis [12]. The next ORR rate determining step is the first electron transfer to oxygen, beginning the electrochemical reaction [13,14]. This step experiences greater inhibition at the basal plane than at the carbon lattice edge. The transfer of the first electron to an adsorbed O_2 molecule is assisted by the presence of nitrogen, but the nitrogen incorporation does not decrease the oxygen adsorption barrier at the lattice edges [11]. A theoretical study has shown that a graphitic nitrogen structure promotes a more substantial ORR catalysis than pyridinic-N [11,15]. This is in stark contrast to the reports of other studies, which suggest that ORR catalysis is promoted mostly at the active sites comprising pyridinic-N bonding [16–18]. Kim et al. (2011) added some clarity to this debate, by noting that oxygen adsorption is facilitated by graphitic-N, while during a 4-electron reduction of oxygen, the same graphitic-N assumes a pyridinic nitrogen structure. Upon the completion of ORR, the graphitic nitrogen is restored [11].

Ammonia, pyridine and urea have been previously observed to disseminate nitrogen into the atomic structure [19–21]. Graphene with a high level of carbon lattice defects can promote a significant incorporation of nitrogen, with the lattice edges being sites of abundant nitrogen recruitment [19,22,23]. The most common bonding types of nitrogen incorporation include graphitic nitrogen, pyridinic nitrogen and pyrrolic nitrogen formation [9,24]. Pyridinic-N involves the binding of nitrogen to two carbon atoms in a 5-carbon atom ring, resulting in the contribution of one p-electron to the π-conjugation system [22,25]. During the formation of graphitic-N, nitrogen acts as an electron donor, enabling a direct substitution of carbon for nitrogen [26]. Pyrrolic-N incorporation involves the transfer of two p-electrons to the π-conjugation system [22,27]. The edges of graphene harbour the highest density of ORR active sites, mostly promoting formation of pyridinic and pyrrolic nitrogen incorporation [28,29].

The majority of the methods disclosed for delivery of single to few layer graphene mostly provide small quantities [5]. Ball milling facilitates a viable mass production route for adjustment of the physical and molecular structure of graphite [30,31]. A change in oxygen electrocatalysis on graphite nanosheets is influenced by adjustment of the particle diameter during ball-milling [32]. After milling of graphite, an overall deterioration of structural order within the individual particulates is observed [33]. Graphene nanoplatelets can exhibit some of the beneficial characteristics of single layer graphene, such as high conductivity, high surface area and significant mechanical strength [34]. Graphene nanoplatelets are ≤10 carbon lattice layers in thickness and exhibit similar properties to that of single or few layer graphene. The starting material used for the production of graphene nanoplatelets is graphite, which favours mass production, due to large quantities of graphite being abundantly available for mining [34]. Ball-milling of graphite produces graphene nanoplatelets which exhibit enhanced electrochemical behaviour [35,36]. Previous work has reported an effective mechanical exfoliation in 1-butyl-3-methylimidazolium hexafluorophosphate (BMIM-PF_6), for the provision of few layered graphenic material from graphite [37]. The BMIM-PF_6 is observed to promote effective dispersion of graphenic particles [38] and has a surface tension similar to graphite surface energy, which prevents the re-attachment of exfoliated carbon lattice layers [37–42]. The current study involves employment of a facile graphite grinding in BMIM-PF_6 for the provision of graphene nanoplatelets, a process which has potential for up-scaled production. This paper also wishes to disclose the oxygen reduction reaction catalysis bestowed by the pristine graphenic material produced using a similar method to that employed by Shang et al. (2012). The subsequent enhancement of ORR catalysis after pyrolytic heat treatment of the graphene nanoplatelet preparations in the presence of urea is also discussed.

2. Experimental

2.1. Material preparation

2.1.1. Production of pristine and N-doped graphene nanoplatelets

Graphite (≤20 μm; fluka) was ground for varied durations in BMIM-PF_6 (Sigma), to provide graphene nanoplatelets. Two main samples are assessed, graphite ground for 30 min (denoted as GP 0.5-hr) and graphite ground for 4 h (denoted as GP 4-hr), respectively, in BMIM-PF_6. Subsequent nitrogen doping was completed in a dry powder sample of graphene nanoplatelets (50 mg) with a mixture of urea to a desired ratio (1:5, 1:10, 1:15, 1:20). The untreated graphite also was pyrolysed with urea, and is denoted as N-graphite 0-hr 600 °C. While the GP 0.5-hr and GP 4-hr samples after pyrolysis treatment are denoted as N-GP 0.5-hr 600 °C and N-GP 4-hr 600 °C, respectively. A ceramic tube furnace purged with N_2 gas was used to pyrolyse the samples under an N_2 flow rate of 1.8 cm^3 min^{-1} for 1 h to the required temperature.

2.1.2. Catalyst coating preparation

For all the samples prepared in this study, the final catalyst powder was prepared in a 5 mg ml^{-1} catalyst ink containing a 1:20 dilution of nafion 117 solution (~5% in a mixture of lower aliphatic alcohols and water; Sigma) in *N*,*N*-dimethylformamide (DMF). The electrode coating was prepared by pipetting this material solution onto a glassy carbon electrode (GCE) disc. For the graphite-derived materials, 6 μl was dispensed onto the GCE disc, creating a 30 μg coating to a density of 0.424 mg cm^{-2}. Platinum on carbon black (Pt/C) coatings were prepared with platinum, which is nominally 20% on carbon black (Alfa Aesar). Pt/C was prepared by adding 4 μl of the material solution to a GCE disc, creating a 20 μg coating to a density of 0.283 mg cm^{-2}. The catalyst ink addition to the GCE disc was then dried gently under an infra-red (IR) lamp.

2.2. Electrochemical characterisation

Voltammetry was performed between +0.2 V and −1.0 V. Linear sweep voltammetry (LSV) was measured at a 10 mV s^{-1} scan rate with an RDE rotation of 1600 rpm unless otherwise stated. Cyclic voltammetry (CV) was taken at a 100 mV s^{-1} scan rate. When applying the Koutecky–Levich (K–L) equation during ORR efficiency assessments, a rotation rate of 225 rpm–3600 rpm was employed. Chronoamperometric analysis was carried out at a rotation rate of 1600 rpm with an applied potential taken from an ORR onset shown in the LSV scan of the material in question. All the electrochemical measurements were conducted in 0.1 M potassium hydroxide (KOH) solution, which was saturated with either O_2 or N_2 as indicated. Electrochemical impedance spectroscopy (EIS) measurements were carried out at a superimposed potential amplitude of 10 mV within a frequency of 10^6 to 10^{-2} Hz. A three electrode set-

up was used for all electrochemical evaluations comprising of a silver/silver chloride (Ag/AgCl) reference electrode, a Pt wire as a counter electrode and a rotating disc GCE (0.0706 cm^2) as a working electrode.

2.3. Material characterisation

Transmission electron microscopy (TEM) images were provided by the JEM-2100F system accessed from Peking University, Beijing, People's Republic of China, which was coordinated by Prof. Meixian Li. Powder samples were prepared on a copper grid before capturing of the TEM images. Atomic force microscopy (AFM) analysis was carried out on the smallest particle portion of each catalyst powder. This was isolated through a settling technique in DMF solution, which was allowed to stand before removal of the supernatant containing the lightest graphene nanoplatelets. These minute particles were then cleansed of DMF through a re-suspension in water and centrifugation, followed by subsequent drying in ambient conditions. A minute quantity of particles were then suspended in acetone and drop-dried onto a silicon substrate. After drying at ambient conditions, the AFM sample coating was analysed in a commercial scanning probe microscope (Dimension 3100, Bruker, US) operated in the tapping mode. Analysis of the data was completed by using Nanoscope Analysis version 1.40 software (Bruker Corporation).

Powder X-ray diffraction (XRD) analysis was obtained using a silicon disc substrate affixed to a X-ray diffractometer system (Bruker D8-Discover diffractometer) with a Cu-Kα radiation source ($\lambda = 1.540$) and a 1st order diffraction ($n = 1$). A He–Ne laser emitted from a Labram system was used to generate the required Raman spectra for the developed samples. The particulate samples were suspended in ethanol, and prepared in a thick coating adhered to a silicon substrate by a drop-drying technique. The coating was then allowed to dry in ambient conditions before Raman analysis. X-ray photoelectron spectroscopy (XPS) surface analysis was facilitated on a Kratos Axis Ultra DLD spectrometer, available at Newcastle University. Analysis of data was completed with Casa XPS software made available through the Newcastle University on-line portal. Samples were prepared as a coating adhered to a silicon substrate by a drop-drying technique while suspended in ethanol. This coated silicon substrate was then loaded onto the XPS stage for analysis under high vacuum conditions.

3. Results and discussion

3.1. Physical appearance and dimensions of the graphene nanoplatelets

Enclosed are TEM images of a single graphene nanoplatelet obtained from the GP 4-hr sample, highlighting the significant decrease in the amount of graphene layers at the edges after 4 h of grinding in BMIM-PF_6 (Fig. 1). The imaged graphene nanoplatelet is isolated from the whole sample after completion of the grinding process and subsequent cleaning to remove the BMIM-PF_6.

Table 1 displays the dimensions measured from 110 nanoplatelets after grinding for 30 min (GP 0.5-hr) and 4 h (GP 4-hr) in BMIM-PF_6, while also showing the resultant nanoplatelet sizes after pyrolytic nitrogen incorporation (N-GP 0.5-hr 600 °C; N-GP 4-hr 600 °C). These nanoplatelets are much smaller than the graphene nanoplatelet imaged by TEM analysis (Fig. 1). This is a result of a separation procedure, which allowed only the smallest fraction of the nanoplatelets to be isolated for AFM measurements, facilitating the report of the most minute dimensions achieved during the production process. The values of Table 1 are obtained from analysis of the completed AFM scans of the pristine GP (Figs. S1 and S2) and N-GP (Figs. 2 and 3) samples. A smaller average particle diameter is observed for the GP 4-hr sample (16.03 nm) and N-GP 4-hr 600 °C sample (18.56 nm) in comparison to the GP 0.5-hr sample (22.51 nm) and N-GP 0.5-hr 600 °C sample (25.84 nm). This indicates that the overall edge length increases in the GP and N-GP samples as the grinding treatment is prolonged before pyrolytic nitrogen doping. Also, the overall surface area of the N-GP sample can be assumed to increase as the measured nanoplatelet diameter and nanoplatelet height decreases. The higher the surface area accessible to the O_2-saturated electrolyte, the more ORR active sites that are utilised during ORR catalysis, promoting further the magnitude of the ORR current response [43].

The height of the nitrogen doped nanoplatelets is an important consideration, as it assists in confirming the occurrence of possible restacking of the nanoplatelets during the heating process. Aggregation and restacking of the carbon lattice layers reduces the surface area of the nanoplatelets, resulting in ORR active N-doping sites being concealed from the O_2-saturated electrolyte, promoting a decrease in electrocatalysis [44]. The AFM results highlight that the maximum nanoplatelet heights are 1.99 nm for the N-GP 4-hr 600 °C sample, while the N-GP 0.5-hr 600 °C sample has a maximum nanoplatelet height of 9.93 nm (Figs. 2 and 3; Table 1).

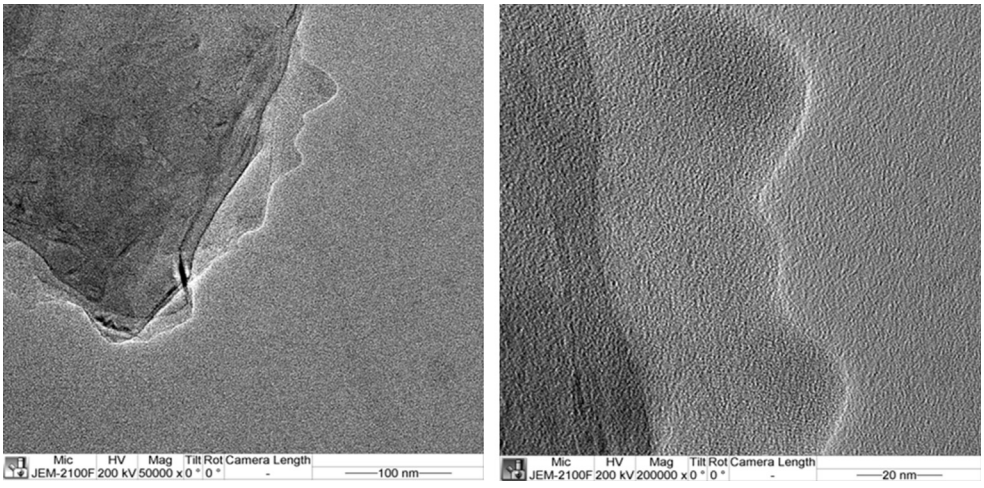

Fig. 1. TEM image of a single graphene nanoplatelet derived from graphite ground in BMIM-PF_6 for 4 h (GP 4-hr).

Table 1
Graphene nanoplatelet geometries from data analysis of 110 nanoplatelets detected during AFM investigation of the smaller particle fraction of the pristine GP (Figs. S1 and S2) and N-GP (Figs. 2 and 3) samples. Graphite samples are ground in BMIM-PF_6 for 30 min (GP 0.5-hr) and 4 h (GP 4-hr) followed by pyrolysis at 600 °C in a 1:10 urea mixing ratio (N-GP 0.5-hr 600 °C; N-GP 4-hr 600 °C).

Sample	Number of particles analysed	Average nanoplatelet height/nm	Minimum nanoplatelet height/nm	Maximum nanoplatelet height/nm	Average nanoplatelet diameter/nm	Minimum nanoplatelet diameter/nm	Maximum nanoplatelet diameter/nm
GP 0.5-hr	110	2.71	1.39	15.18	22.51	11.01	58.43
GP 4-hr	110	0.78	0.45	4.21	16.03	10.44	36.76
N-GP 0.5-hr 600 °C	110	3.89	1.94	9.93	25.84	11.01	65.67
N-GP 4-hr 600 °C	110	0.69	0.40	1.99	18.56	11.01	39.73

Before incorporation of nitrogen, a maximum nanoplatelet height of 4.21 nm is observed for the GP 4-hr sample and 15.18 nm for the GP 0.5-hr sample. These results suggest no significant restacking of the nanoplatelets occurring during pyrolysis or the subsequent post-treatment drying [45], thus allowing optimum surface area for ORR catalysis to be provided.

Single layer graphene has been observed to provide a thickness of ~0.3–1 nm [34,46]. With this considered, the minimum nanoplatelet heights measured in the current study (1.94 nm: N-GP 0.5-hr 600 °C; 0.40 nm: N-GP 4-hr 600 °C) support the presence of few to single-layered graphene nanoplatelets (Table 1). Few to single layer graphene nanodots are indicated to be generated to a minute

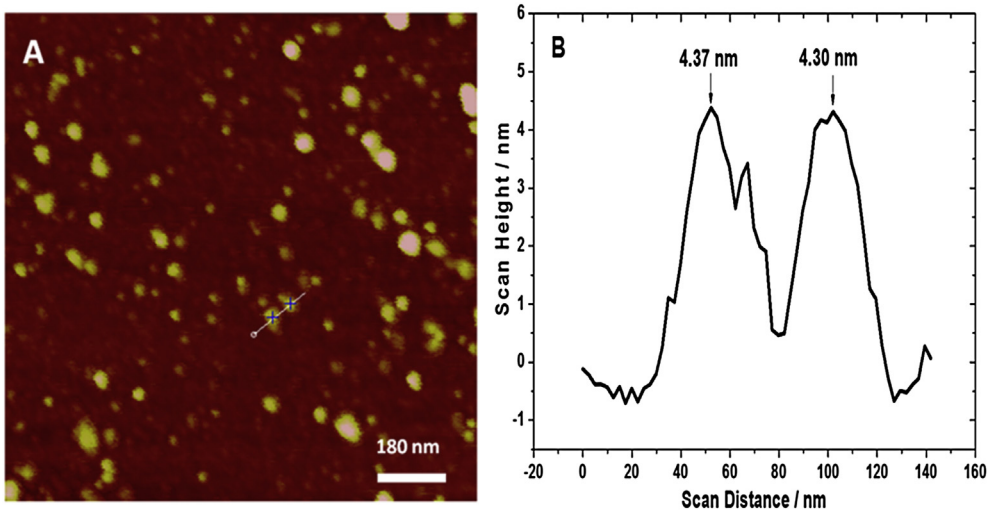

Fig. 2. AFM image of the N-GP 0.5-hr 600 °C sample obtained from graphite ground for 30 min followed by 600 °C pyrolysis in a 1:10 urea mixing ratio. Blue crosses show the position of the nanoplatelets measured (B) along the profile axis indicated by a white line in the centre of the AFM image (A). AFM image scan width is 1 μm. (For interpretation of the references to colour in this figure legend, the reader is referred to the web version of this article.)

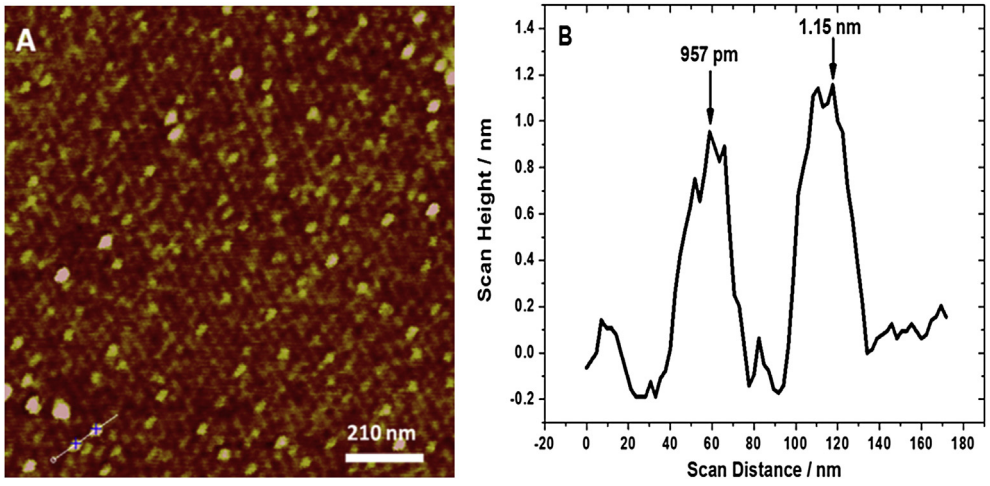

Fig. 3. AFM image (A) of the N-GP 4-hr 600 °C sample produced from grinding of graphite for 4 h with subsequent pyrolysis at 600 °C in a 1:10 urea mixing ratio. The positions of the two nanoplatelets measured in the profile graph (B) are indicated by two blue crosses along the white line profile axis in the bottom right-hand corner of the AFM image (A). AFM image scan width is 1 μm. (For interpretation of the references to colour in this figure legend, the reader is referred to the web version of this article.)

degree in both the pristine and N-doped graphene nanoplatelet samples of this study (Table 1). Graphene nanodots being previously reported to have a diameter of less than 100 nm, while diameters as low as 5–15 nm have also been recorded [47,48]. Whereas the diameter of graphene nanoplatelets is seen to have a range of 1 μm–50 μm [49].

3.2. Elucidation of structural changes on graphene nanoplatelets as a consequence of varied grinding duration and pyrolytic nitrogen incorporation

XRD and Raman spectroscopy data is used to detect a change in the micro-structure of carbon-based materials [50]. Fig. 4 shows the XRD analysis of the pristine GP and N-GP samples considered. The notable increase in the full width-half maxima (FWHM) of the 002 carbon peak (2θ of ~26°) is caused by a decrease in the nanoplatelet size as the grinding duration is prolonged (Table 2).

XRD analysis can facilitate definitive measurement of the distance between the single carbon lattice layers (d-spacing) within a carbon-based planar structure. [51,52] The d-spacing remained unchanged after grinding of graphite (3.3 Å) and subsequent pyrolytic nitrogen incorporation. This consistency in the d-spacing is indicated (Fig. 4) by the 002 carbon peak being present at a 2θ angle of ~26.48° for all of the GP and N-GP samples, which is similar to the position of the untreated graphite starting material (26.47°). The narrow width of the 002 peak suggests that there are large domains parallel and perpendicular to the c-axis of the crystalline structure [53]. The increase in the FWHM of the 002 carbon peak indicates an increase in the boundary length between particles [54,55]. This effect appears to occur for the graphene nanoplatelet samples of this study. An increase in the boundary length between the graphene nanoplatelets is suggested to occur due to the decrease in the nanoplatelet diameter (Table 1) after prolonging of the graphite grinding duration in BMIM-PF_6. The smaller the diameter of the graphene nanoplatelets, the longer the overall boundary length for a given sample.

Raman spectroscopy is a vital component in the area of carbon-based material characterisation. Raman spectra of graphenic materials provides a characteristic signature. A G-band exists at ~1580 cm^{-1}, most common in single graphite crystals, while a 1st order D-peak appears at ~1350 cm^{-1}, when disorder and defects are present in the sp^2 carbon lattice [56]. The G-peak represents the E_{2g} phonon vibration mode, while the D-peak represents the A_{1g} mode of vibrations [56,57]. The second order 2-D peak is also present

Table 2
Highlighting the effect of prolonging the grinding duration and subsequent nitrogen incorporation on the XRD 002 peak FWHM of the starting graphite material (Graphite 0-hr), pristine GP (GP 0.5-hr, GP 4-hr) and the N-GP (N-GP 0.5-hr 600 °C, N-GP 4-hr 600 °C) preparations.

Sample	002 peak FWHM/°
Graphite 0-hr	0.264
GP 0.5-hr	0.270
GP 4-hr	0.280
N-GP 0.5-hr 600 °C	0.260
N-GP 4-hr 600 °C	0.274

at ~2650 cm^{-1}, and is clearly apparent in graphitic and graphenic materials. The 2-D peak FWHM and intensity can be affected by the number of layers of the graphite-based material being analysed [58], which is notable with the presence of graphenic material with 5 carbon lattice layers or less. The 2-D peak is also an indication of the level of structural disorder, with a well defined 2-D peak indicative of a highly ordered carbon lattice structure with low defects [59]. While an absent or highly attenuated 2-D peak indicates a high level of disorder [60]. The D' peak results from structural defects within the carbon lattice as does the D-peak [61]. For the present study, the defects are mostly due to the graphene nanoplatelet edges, where disorder in the carbon bonding structure is widespread. The developed samples were measured while coated onto a silicon substrate by a simple drop-drying technique. This allows simulation of the orientation of the GP and N-GP samples as they would be displayed on the GCE disc during electrochemical assessment, as the catalyst ink was deposited by a drop-drying technique before all electrochemical analyses. This simulation allows a closer correlation to the structural aspects apparent from Raman spectroscopy data to the observed electrochemical behaviour from the individual GP and N-GP samples developed.

A decrease in nanoplatelet size and an increase in the surface defect density is indicated by an I_D/I_G ratio increase in the Raman spectra [62,63]. The graphene nanoplatelets for the GP 4-hr sample are indicated to have a higher level of surface defects and a smaller nanoplatelet size ($I_D/I_G = 0.79$) in comparison to the graphite 0-hr ($I_D/I_G = 0.32$) and GP 0.5-hr samples ($I_D/I_G = 0.76$) (Fig. 5). This is due to the increase in the edge length exposure caused by the decrease in the diameter of the graphene nanoplatelets during a prolonged grinding duration.

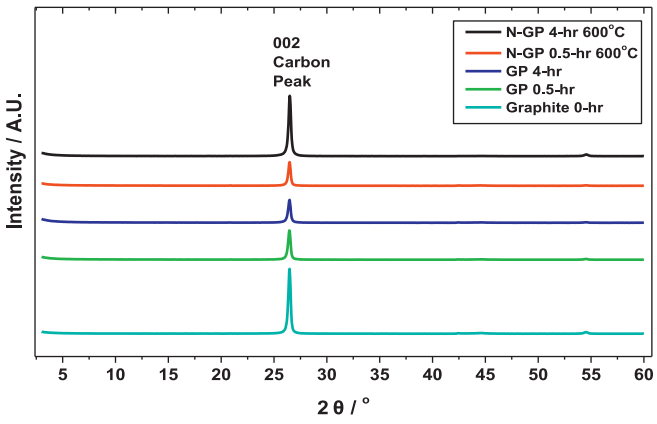

Fig. 4. XRD spectra of pristine GP samples (GP 0.5-hr, GP 4-hr) produced by grinding of graphite for 30 min and 4 h which were then subsequently pyrolysed at 600 °C in a 1:10 urea mixing ratio to deliver N-doped GP samples (N-GP 0.5-hr 600 °C; N-GP 4-hr 600 °C). For comparison untreated graphite is also shown (Graphite 0-hr).

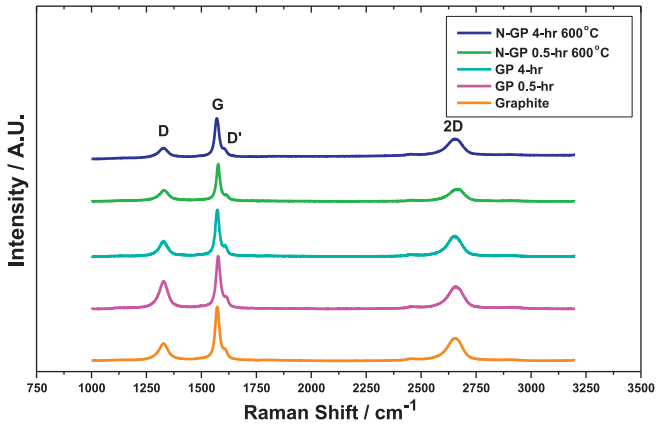

Fig. 5. Raman spectroscopy data of the graphite starting material (Graphite 0-hr) along with pristine GP (GP 0.5-hr, GP 4-hr) and N-GP samples produced from BMIM-PF_6 assisted graphite grinding for 30 min (N-GP 0.5-hr 600 °C) and 4 h (N-GP 4-hr 600 °C), respectively, followed by pyrolysis at 600 °C in the presence of a 1:10 mixing ratio with urea.

In Fig. 5, the Raman spectra for the N-doped samples also indicates an increase in I_D/I_G ratio as the graphite grinding duration increases before nitrogen incorporation (N-GP 4-hr 600 °C sample: I_D/I_G ratio = 0.88, N-GP 0.5-hr 600 °C: I_D/I_G = 0.86). This increase in the I_D/I_G ratio corresponds to a decrease in particle size with prolonged grinding duration, causing an increase in the display of the edge plane defects from the sample even before pyrolytic treatment with urea [63,64]. Nitrogen incorporation also induces an increased level of defects into the carbon lattice [65], which contributes to the I_D/I_G ratio increase observed after pyrolytic treatment.

3.3. Composition of graphene nanoplatelets as a result of varied grinding duration

XPS analysis of carbon-based materials possess two basic electronic spectra consisting of a photoemission line of C1s and a CKLL Auger line [66]. The most common hybridisation types for carbon materials are sp^3 (diamond-like, s-bonding) and sp^2 (graphite-like, weak p-bonds) symmetries [67,68], with significant levels of both found in amorphous carbon [66]. The sp^3 bonds present in sp^2 carbon lattices are usually a result of defects being induced in the atomic structure. Figs. S3 and S4 confirm the presence of C1s at 284.5 eV in the pristine and N-doped sample preparations, indicative of a graphite-like sp^2 honeycomb carbon lattice [19]. The C1s peak being typically asymmetric in graphite-based materials [69]. While an O1s peak is present in the starting graphite and the GP and N-GP samples (Figs. S3 and S4). Nitrogen incorporation is higher in the N-GP 4-hr 600 °C sample (4.44 at.%) while a lower level is present in the N-GP 0.5-hr 600 °C (1.10 at.%) and N-graphite 0-hr 600 °C (1.11 at.%) samples (Fig. 6). After incorporation of nitrogen into the graphene carbon lattice, the electrical conductivity decreases and the band gap between the conduction band and the valence band is larger than that of pristine graphene [19,24,70]. A possible reason for this decrease in conductivity being the increase in topological defects which facilitate scattering centres [19]. Also apparent is a minute Auger peak ($OKL_{23}L_{23}$), induced by the oxygen content of the carbon lattice with the carbon Auger peak ($CKL_{23}L_{23}$) being even more pronounced (Figs. S3 and S4).

Table 3 allows a definitive confirmation of the distribution of the nitrogen bonding types shown as a percentage of the entire nitrogen content detected for the individual N-doped samples assessed.

The dominance of pyridinic-N (~398 eV) [27,71] among the samples analysed, correlates with the most improved ORR catalytic response provided by N-GP 4-hr 600 °C sample (Table 3). The N-GP 0.5-hr 600 °C and N-graphite 0-hr 600 °C samples have pyrrolic-N (400.1 eV) [25,27] as the dominant nitrogen bonding type and provide a lower ORR catalysis (Table 3). While both N-GP 0.5-hr 600 °C and N-GP 4-hr 600 °C samples have graphitic-N (401.7 eV) [27] as the lowest nitrogen functional group. Pyridinic-N facilitates O_2 adsorption to the carbon lattice surface, which promotes maximum availability of O_2 during ORR catalysis at the site of incorporation [18,72]. The overall atomic percentage of nitrogen differs significantly as indicated in Table 4.

The increase in the grinding duration before pyrolysis is indicated to promote a higher incorporation of nitrogen, with the most significant improvement in ORR catalysis occurring in the GP 4-hr sample after reaction with urea (Table 4; Figs. 8, 9 and 12). The

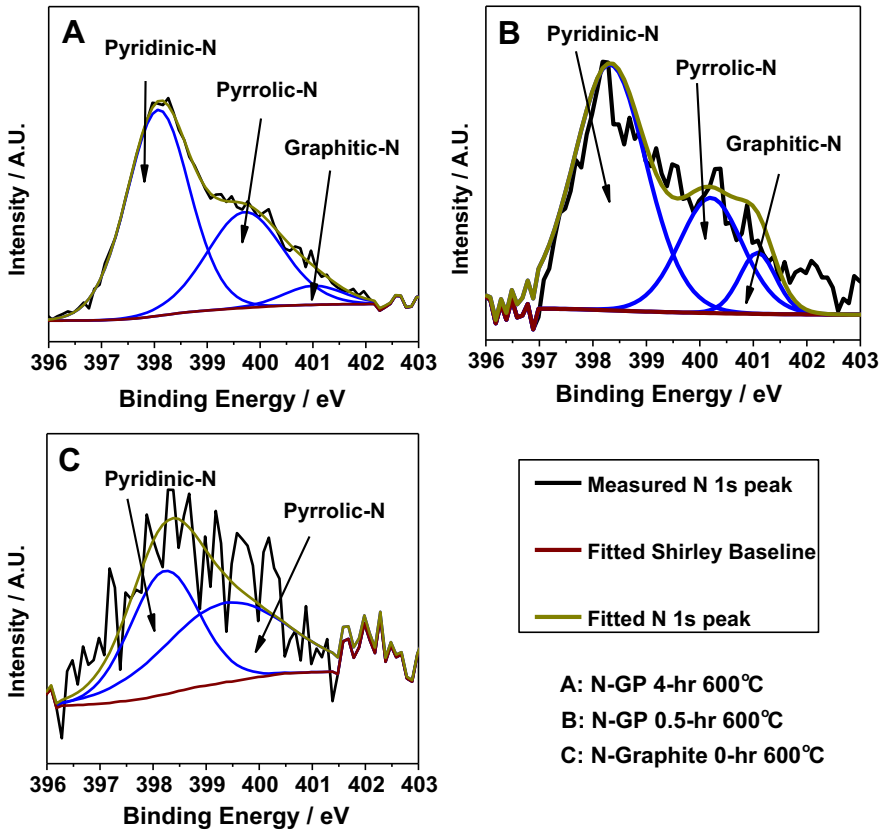

Fig. 6. XPS results showing a deconvoluted N1s spectra for the N-GP samples which is produced from graphite grinding for 30 min and 4 h followed by pyrolysis at 600 °C with a 1:10 urea mixing ratio (N-GP 0.5-hr 600 °C; N-GP 4-hr 600 °C). Also displayed is graphite starting material, which is not ground but N-doped with the same procedure (N-graphite 0-hr 600 °C) as the N-GP samples for comparison purposes.

Table 3
Highlighted is the effect on the abundance of the different types of incorporated nitrogen bonds formed during pyrolysis of graphite-derived material and urea. All N-GP (N-GP 0.5-hr 600 °C, N-GP 4-hr 600 °C) and N-graphite (N-Graphite 0-hr 600 °C) samples are pyrolysed in a tube furnace with a 1:10 powder mixture of graphite-derived material and urea at 600 °C in a N_2-saturated environment.

Sample material	Pyridinic-N/% of total nitrogen	Pyrrolic-N/% of total nitrogen	Graphitic-N/% of total nitrogen
N-GP 4-hr 600°C	69.16	29.02	1.82
N-GP 0.5-hr 600°C	26.72	65.16	8.12
N-graphite 0-hr 600 °C	46.83	53.17	–

Table 4
Atomic percentage values for carbon (C1s), nitrogen (N1s) and oxygen (O1s) content of the N-doped samples produced by grinding graphite for 30 min and 4 h followed by pyrolysis at 600 °C in a 1:10 urea ratio (N-GP 0.5-hr 600 °C, N-GP 4-hr 600 °C). N-graphite 0-hr 600 °C sample is produced from untreated graphite particles, which received the same pyrolysis procedure as the N-GP preparations.

Sample material	C1s/atomic %	N1s/atomic %	O1s/atomic %
N-GP 4-hr 600°C	93.03	4.44	2.51
N-GP 0.5-hr 600°C	97.14	1.10	1.75
N-graphite 0-hr 600°C	95.21	1.11	3.68

type of nitrogen bonding structure, as well as the degree of incorporation, play an important role in modulating the catalytic properties of graphene (Tables 3 and 4) [19,73].

3.4. Linear sweep voltammetry analysis of ORR electrocatalysis

The onset of ORR at ~−0.1 V (Fig. 7) is indicated by a sharp increase in the cathodic current, which comprises the initial 2-electron reduction of oxygen in alkaline conditions to the perhydroxyl radical (HO_2^-) and a hydroxide anion (OH^-) (Equation (1)) [74,75]. The second reaction onset at ~−0.7 V, is the second stage of ORR (Equation (2)), involving the reduction of the perhydroxyl radical and water to hydroxide anions [74,75]. This second reaction onset would not be clearly observable where the ORR is a single 4-electron reaction step, as is seen in Fig. 11 for the LSV scan taken of Pt/C in 0 M methanol. [76]

$$O_2 + H_2O \rightarrow HO_2^- + OH^- \quad (1)$$

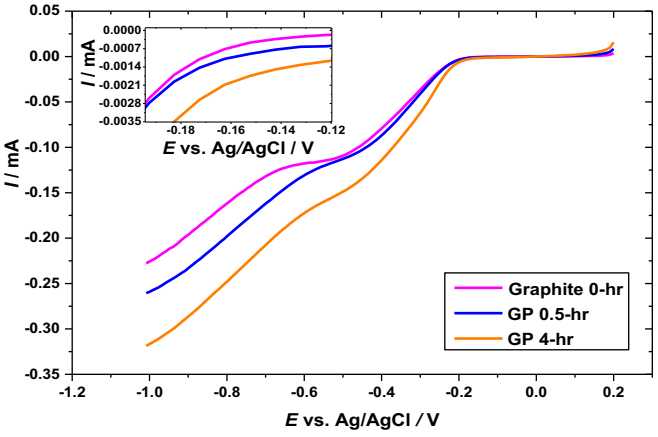

Fig. 7. Linear sweep voltammograms shown of graphite ground in BMIM-PF_6 for 30 min (GP 0.5-hr) and 4 h (GP 4-hr). Untreated graphite is also included for comparison (Graphite 0-hr). Material is prepared in a 0.424 mg cm^{-2} coating on a GCE disc (0.0706 cm^2) in an O_2-saturated 0.1 M KOH electrolyte. Scan rate is 10 mV s^{-1} and the step potential is 10 mV.

$$HO_2^- + H_2O \rightarrow 3OH^- \quad (2)$$

In Fig. 7, graphite starting material (graphite 0-hr) shows the lowest ORR response with a cathodic current of 0.117 mA (1.65 mA cm^{-2}) at −0.6 V, together with the most negative ORR onset potential (−0.187 V) of the comparison shown. After 30 min of grinding graphite in BMIM-PF_6, the GP 0.5-hr sample shows a slight increase in ORR cathodic current with a value of 0.13 mA (1.84 mA cm^{-2}) at −0.6 V. The GP 4-hr sample shows an improvement in the ORR current response (0.171 mA (2.42 mA cm^{-2}) at −0.6 V) and ORR onset potential (−0.163 V) in comparison to that of untreated graphite (−0.187 V) or the GP 0.5-hr sample (−0.184 V).

Previously, graphite milled with stainless steel ball bearings in the presence of hydrogen (−0.24 V) and carboxylic acid (−0.22 V) displayed a more negative onset potential compared with the LSV analysis of the GP 0.5-hr and GP 4-hr samples of the current investigation [35]. Another study reported the production of acylated graphene nanoplatelets, which catalyse ORR in alkaline conditions [36,44], providing an ORR onset potential of ~−0.180 V and an ORR current density of 0.5 mA cm^{-2} at −0.6 V [44]. These previous studies highlight the advantage provided by the BMIM-PF_6 assisted graphite grinding production of the pristine GP samples (GP 0.5-hr (ORR onset: −0.184 V; 1.84 mA cm^{-2} at −0.6 V), GP 4-hr (ORR onset: −0.163 V; 2.42 mA cm^{-2} at −0.6 V)) (Fig. 7). Formation of active sites to the edges of the carbon lattice are facilitated by the high level of unpaired electrons, which lack abundance on the basal plane [77–79]. The lower performance of the acetylated graphene nanoplatelets is speculated to be a result of the termination of the carbon lattice layers with acyl groups, which inhibit the electrochemically active edges [77,78]. The BMIM-PF_6 prevents re-attachment of the exfoliated layers [37], which promotes the abundance of minute nanoplatelets. The increased abundance of minute nanoplatelets displaying a higher degree of defect-rich edges to the electrolyte, translating into a high amount of electrochemically active sites [80].

3.5. Optimisation of ORR catalysis by incorporation of nitrogen into the GP carbon lattice

Observed from a previous report is an improved ORR catalysis behaviour from variation of the ratio of urea mixed with graphenic material during heat treatment [81]. This prompted an investigation to determine the optimum ratio of GP: urea powder allowing greatest enhancement of ORR catalysis after pyrolytic heat treatment. As the GP 4-hr sample provided the highest ORR magnitude, urea mixing ratios of 1:5 (50 mg:250 mg), 1:10 (50 mg:500 mg), 1:15 (50 mg:750 mg) and 1:20 (50 mg:1000 mg) have been assessed and it is found that the 1:10 urea mixing ratio results in the most enhanced ORR onset potential (−0.081 V) during LSV analysis (Fig. S15(A)). The N-GP 4-hr 600 °C sample from a 1:10 ratio of GP: urea pyrolysis provided an ORR current at −0.6 V of 0.225 mA (3.186 mA cm^{-2}), while the 1:5, 1:15 and 1:20 urea treatment ratios have a lesser current magnitude at −0.6 V of 0.186 mA (2.634 mA cm^{-2}), 0.177 mA (2.507 mA cm^{-2}) and 0.154 mA (2.181 mA cm^{-2}), respectively (Fig. S15(A)). The maximum current obtained from the peak just after ORR onset during CV analysis being 0.0836 mA (1.184 mA cm^{-2}) for the 1:10 ratio, while the 1:5, 1:15 and 1:20 urea mixing ratios applied during pyrolysis provided a maximum current of 0.06 mA (0.849 mA cm^{-2}), 0.074 mA (1.048 mA cm^{-2}) and 0.082 mA (1.161 mA cm^{-2}), respectively (Fig. S15(B)). The more positive the ORR peak observed after catalysis onset during CV analysis, the more efficient the ORR and the less overpotential required to

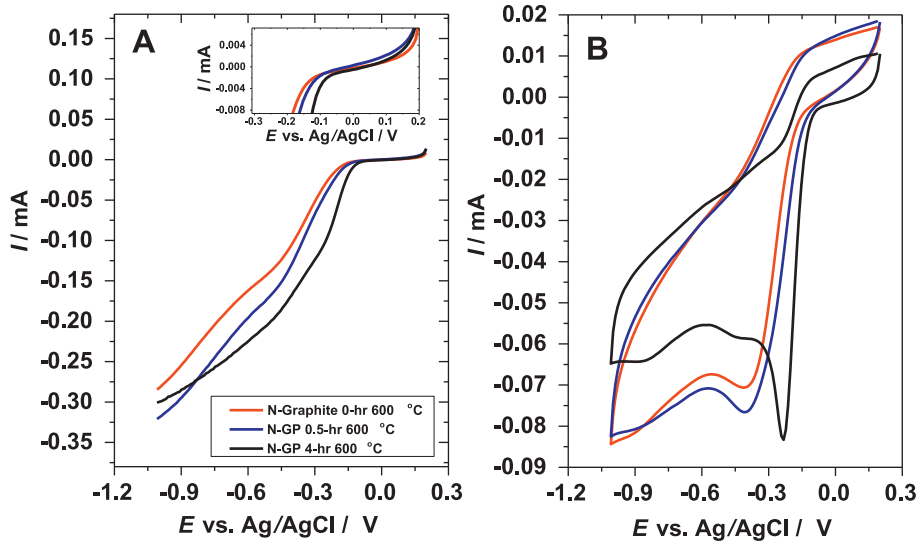

Fig. 8. LSV (A) and CV (B) scans highlighting the increase of the cathodic current response as a result of prolonging graphite grinding in BMIM-PF_6 with subsequent nitrogen doping during pyrolysis at 600 °C in a 1:10 powder mixture of graphite derived material with urea. A comparison of N-graphite 0-hr 600 °C sample (red) with no grinding before pyrolysis is shown with N-GP 0.5-hr 600 °C (blue) and N-GP 4-hr 600 °C (black) samples. Sample loading on the GCE disc (0.0706 cm^2) is 0.424 mg cm^{-2}. (For interpretation of the references to colour in this figure legend, the reader is referred to the web version of this article.)

initiate the reaction. The ORR peak current position is −0.233 V for CV analysis of the N-GP 600 °C 1:10 ratio sample, in contrast to the more negative potentials for the ORR peak position of the 1:5(−0.298 V), 1:15(−0.409 V) and 1:20(−0.317 V) urea ratios used during pyrolysis. These results suggest that the highest magnitude of ORR catalysis from the samples studied occurs for the N-GP 4-hr 600 °C sample fabricated from pyrolysis in the presence of urea to a mixing ratio of 1:10 (Fig. S15).

The dissociation of urea results in nitrogen rich by-products such as ammonia (NH_3) and isocyanic acid (HNCO), which upon further dissociation may allow the incorporation of nitrogen into the carbon lattice structure [82–84]. If a significant amount of urea was not contacting the N-GP sample upon dissociation, as may have occurred for the sample produced from pyrolysis of a 1:5 GP: urea mixing ratio, then this may inhibit the overall incorporation of nitrogen and the formation of any subsequent carbon lattice defects acting as ORR active sites. Also, the 1:15 and 1:20 GP: urea mixing ratios could possess too high a number of active sites after pyrolysis inferring high carbon lattice disorder. A high defect density could inhibit charge carrier mobility as previously suggested by Wu et al. (2013), which may decrease ORR efficiency [81]. Whereas the 1:5 mixing ratio could provide a lower defect density and nitrogen incorporation than that observed in the N-GP sample derived after pyrolysis of a 1:10 GP: urea powder ratio, explaining the decrease in ORR catalysis [81].

Pyrolysis temperatures of 400 °C, 500 °C, 600 °C and 700 °C are used on a GP: urea mixing ratio of 1:10 to confirm the most effective pyrolysis temperature for enhancement of ORR catalysis. The LSV analysis of the N-GP 4-hr 600 °C sample (−0.081 V) needed the least overpotential for ORR initiation in comparison to the equivalent treatments at 400 °C(−0.171 V), 500 °C (−0.127 V) and 700 °C(−0.125 V) (Fig. S16(A)). The ORR peak position provided during CV analysis for the N-GP 4-hr 600 °C 1:10 sample (−0.233 V) is significantly more positive than the ORR peak position observed from CV analysis of N-GP 4-hr samples pyrolysed at 400 °C (−0.306 V), 500 °C (−0.344 V) and 700 °C (−0.328 V) (Fig. S16(B)). The more positive the ORR peak in a CV scan, the less overpotential required for catalysis. N-GP 4-hr 600 °C sample derived from a 1:10 mixing ratio is shown from CV analysis (Fig. S16(B)) to have an ORR onset potential of −0.192 V, −0.154 V, −0.104 V, −0.153 V from pyrolysis at 400 °C, 500 °C, 600 °C and 700 °C treatment, respectively. This further supports the finding that the least overpotential is required for ORR initiation from the N-GP 4-hr sample produced at 600 °C during pyrolysis. The temperature of pyrolysis at which optimum ORR catalysis is obtained from the N-GP 4-hr sample is in contrast to other N-graphenic samples provided by Yang et al. (2012), reporting optimum ORR catalysis after the delivery of nitrogen doped reduced graphene oxide at 900 °C. [42] This highlights the higher energy efficiency of the currently proposed production strategy. The N-doped reduced graphene oxide samples of Yang et al. (2012) were synthesised from graphene oxide coated with porous silica layers. Silica is a known insulator [85] and appears to inhibit the heating and incorporation of nitrogen, which is an issue that is averted by the current study.

The heat treatment and GP: urea mixing ratios are confirmed to provide optimum ORR catalysis with a 600 °C pyrolysis of GP 4-hr at a ratio of 1:10 mixing with urea (Figs. S15 and S16). With this information, a meaningful comparison can be sought of the influence on ORR catalysis from varying the graphite grinding duration before pyrolysis. Fig. 8(B) shows the ORR onset potential during CV analysis sequentially moving to a more positive potential as the grinding is prolonged (N-graphite 0-hr 600 °C, −0.160 V; N-GP 0.5-hr 600 °C, −0.131 V; N-GP 4-hr 600 °C, −0.104 V)(Fig. 8(B)). The ORR onset potential observed during LSV analysis of the N-GP samples (N-GP 0-hr 600 °C, −0.125 V; N-GP 0.5-hr 600 °C, −0.111 V; N-GP 4-hr 600 °C, −0.081 V) behaves in a similar fashion (Fig. 8(A)). The ORR peak position for the CV analysis of N-graphite 0-hr 600 °C (−0.417 V) and N-GP 0.5-hr 600 °C (−0.408 V) samples is noted to occupy a similar potential (Fig. 8(B)). The N-GP 4-hr 600 °C sample allows the most positive voltage for the positioning of the ORR peak in the CV data (−0.233 V) (Fig. 8(B)).

The ORR cathodic current increases at −0.6 V during LSV analysis as the grinding duration before pyrolysis was prolonged (N-graphite 0-hr 600 °C, 0.164 mA (2.322 mA cm^{-2}); N-GP 0.5-hr 600 °C, 0.198 mA (2.804 mA cm^{-2}); N-GP 4-hr 600 °C, 0.225 mA (3.186 mA cm^{-2})). The cathodic current at the ORR peak in the CV analysis (Fig. 8(B)) also increased with a longer grinding duration of the sample (N-graphite 0-hr 600 °C, 0.070 mA (0.991 mA cm^{-2}); N-GP 0.5-hr 600 °C, 0.076 mA (1.076 mA cm^{-2}); N-GP 4-hr 600 °C, 0.083 mA (1.175 mA cm^{-2})). These findings suggest that the

increased edge exposure, resulting from the decrease of the nanoplatelet diameter (Table 1) after prolonged grinding promotes ORR catalysis (Fig. 7). Provision of carbon defects at the edge plane of the pristine GP samples is believed to be a secondary contribution to ORR catalysis. The main benefit of the edge plane increase is speculated to be the increased availability of abundant nitrogen incorporation positions, promoting a higher level of ORR active sites (Fig. 8; fig. S5) [86].

To further confirm the actual cathodic current magnitude from ORR catalysis, CV analysis is carried out in N_2-saturated 0.1 M KOH electrolyte and compared to the O_2-saturated 0.1 M KOH measurements (Fig. 9). Measuring the maximum ORR current response using a N_2-saturated CV scan as a baseline is a more accurate consideration of actual ORR current produced.

Optimum pyrolysis conditions of a mixing ratio of 1:10 graphite/GP: urea at 600 °C treatment is used to create the N-graphite and N-GP samples shown in the CV data of Fig. 9. Only after a significant prolonging of grinding for 4 h, does the ORR catalytic current noticeably improve after pyrolytic nitrogen incorporation (Fig. 9). This is confirmed with a maximum ORR current of ~0.06 mA (0.84 mA cm^{-2}) for the N-graphite 0-hr 600 °C and N-GP 0.5-hr 600 °C samples, while the ORR current is 0.079 mA (1.11 mA cm^{-2}) for the N-GP 4-hr 600 °C sample (Fig. 9).

A report by Qu et al., (2010) disclosed that single layer N-graphene sheets have shown an onset potential of ~−0.15 V vs. Ag/AgCl reference electrode during LSV analysis [7]. This is clearly less promising than the onset potential obtained during LSV analysis from the N-GP 4-hr 600 °C sample (−0.081 V) (Fig. 8). The improved ORR onset potential for the N-GP 4-hr 600 °C sample is assisted by a high level of defects (Raman spectroscopy $I_D/I_G = 0.88$) at the surface, while the N-graphene reported by Qu et al., (2010) is shown to have a lower defect density ($I_D/I_G = 0.06–0.25$) [7,80]. The ORR onset potential during LSV analysis of a previously disclosed preparation of Poly-Dimethyldiallylammonium Chloride (PDDA) modified graphene is −0.12 V vs. SCE (saturated calomel electrode) (~−0.11 V when calculated for a Ag/AgCl (1 M KCl) reference electrode) [87]. This enhanced ORR catalysis is a result of the intermolecular charge transfer facilitated after PDDA adsorption, causing an overall positive charge at the carbon atoms [87]. The developed N-GP 4-hr 600 °C sample of the current study, provides a more promising ORR onset during LSV analysis (−0.081 V), promoted by the enhanced ORR catalysis bestowed after the incorporation of nitrogen [88,89].

Clearly graphitic-N, [11,15] pyridinic-N, [16–18,72,90] and pyrrolic-N, [91] bestow an increase in ORR catalysis at the surface of graphene-based electrocatalysts. The actual ORR active site does not simply consist of an added constituent, but of carbon atoms adjacent to the incorporated nitrogen atom, which were part of the lattice before nitrogen doping. These carbon atoms having their electronic configuration modified by an adjacent nitrogen functional group created after pyrolysis [92]. The modified electronic configuration of the carbon atom promotes the adsorption of oxygen. It is believed that the majority of the ORR active sites occur at the edge plane of the N-GP samples, indicated by the significant amount of pyridinic-N and pyrrolic-N, which favour formation at the termination of the carbon lattice [11,19,93]. Kim et al. (2011) proposes that the 4-electron ORR pathway most easily occurs at the graphitic-N next to the carbon lattice edge and is inhibited more so at the graphitic-N upon the basal plane. This being partly due to the carbon lattice edge being inherently more electrochemically active than the basal plane [80]. The location of the graphitic-N incorporation is undecipherable due to XPS being unable to identify the location of the incorporation [94]. The highest level of edge plane exposure being indicated from the N-GP 4-hr 600 °C sample, making it highly possible that the presence of the graphitic nitrogen occurs mostly at the carbon lattice edge, together with pyridinic and pyrrolic nitrogen bonding. This highest edge plane exposure being indicated by the smaller average, minimum and maximum diameters of the N-GP 4-hr 600 °C nanoplatelets (Table 1). The N-graphite 0-hr 600 °C sample has similar nitrogen incorporation content to that of the N-GP 0.5-hr 600 °C sample, but a lower ORR catalysis activity due perhaps to the lack of graphitic nitrogen next to the carbon lattice edges (Table 3). This would decrease the ORR active sites next to the edges of the N-graphite 0-hr 600 °C sample to a lower level than the N-GP 0.5-hr 600 °C sample.

Fig. 10(A) shows a Nyquist plot of the impedance response determined from the N-GP 4-hr 600 °C sample in comparison to the N-GP 0.5-hr 600 °C sample. A change in the imaginary impedance (Z'') is shown in relation to the real impedance (Z'), in response to a

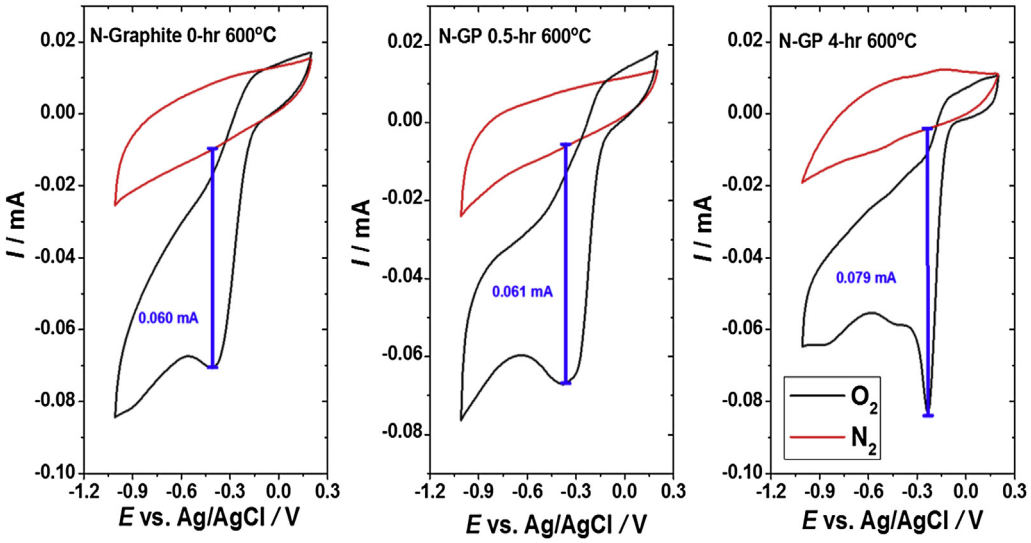

Fig. 9. CV scans of untreated graphite, graphite ground for 30 min and graphite ground for 4 h followed by pyrolysis at 600 °C in a 1:10 urea powder mixture, denoted as N-graphite 0-hr 600 °C, N-GP 0.5-hr 600 °C and N-GP 4-hr 600 °C, respectively. Measurements are of a 0.424 mg cm^{-2} coating on a GCE disc (0.0706 cm^2) in O_2-saturated (black) and N_2-saturated (red) 0.1 M KOH electrolyte. CV scan rate is 100 mV s^{-1} with a step potential of 10 mV.

frequency scan (10^6–10^{-2} Hz) of the alternating potential applied during EIS analysis. The diameters of the curves shown in the lower frequency region of the Nyquist plot represents the charge transfer resistance experienced at the surface of the electrode being analysed during the promotion of ORR catalysis [95]. From observation of the Nyquist plot, the diameter of the curve from the N-GP 0.5-hr 600 °C sample is seen to be larger than the diameter of the curve of the N-GP 4-hr 600 °C sample analysis. This is due most probably to the higher abundance of ORR active sites at the surface of the N-GP 4-hr 600 °C sample, caused by the higher incorporation of nitrogen (4.44 at.% N 1s) in comparison to the N-GP 0.5-hr 600 °C sample (1.11 at.% N 1s). The higher efficiency and magnitude of ORR catalysis occurring at the N-GP 4-hr 600 °C sample instigating a lower overall charge transfer resistance during EIS analysis. While the charge transfer resistance is much higher at the surface of the N-GP 0.5-hr 600 °C sample, due to the lower ORR catalysis magnitude and efficiency at the electrode–electrolyte interface. This explaining the wider diameter of the curve observed at the lower frequency range of the Nyquist plot for the N-GP 0.5-hr 600 °C sample (Fig. 10).

No rotation of the working electrode is employed during EIS analysis, allowing measurement conditions to resemble that of CV analysis (Fig. S13). In Fig. 10, EIS data was measured at −0.1 V and considering the CV analysis at this applied potential, indicates a higher cathodic current from the N-GP 4-hr 600 °C sample than the N-GP 0.5-hr 600 °C sample (Fig. S13: inset). The enhanced ORR after 4 h of grinding being a cause for the lower level of capacitive imaginary impedance observed in the lower frequency range (~10^0–10^{-2} Hz) of the Nyquist plot (Fig. 10(A)). The overall impedance modulus decreases at the N-GP surface between 10^0–10^{-2} Hz as a result of the higher ORR catalysis provided (Fig. 10(B)). This is further confirmed by comparison of the EIS analysis measured at an applied potential before (+0.01 V) and after (−0.1 V) ORR catalysis onset as observed during CV analysis of the same electrode coating (Figs. S13, Fig. S14(C) and Fig. S14(D)). Before ORR onset, at +0.01 V, the capacitive imaginary impedance is high in the Nyquist plot (Fig. S14(A) and Fig. S14(B)) of both the N-GP 4-hr 600 °C sample and the N-GP 0.5-hr 600 °C sample. While at −0.1 V, after initiation of ORR onset (Fig. S13), a lower imaginary impedance is displayed in the Nyquist plot, indicating a charge transfer resistance component is more apparent (Fig. S14(A) and Fig. S14(B)). This being most likely a result of the electron transfer increase across the electrode–electrolyte interface inferred by ORR catalysis.

3.6. ORR kinetic efficiency evaluation of the N-GP samples

The improvement in ORR catalysis is clear after pyrolysis of the GP samples in the presence of urea. Figs. S6 and S8 shows the LSV scans allowing calculation of the number of electrons transferred per reduced oxygen molecule for the developed samples. The efficiency of the ORR for facilitating a cathodic current is clarified through application of the K–L equation, which is employed to confirm the electron transfer number (n) [96,97]. The K–L analysis was primarily constructed to assess the electron kinetics at the surface of a planar electrode [98–100]. As reported from previous studies, the K–L equation is successful in calculating the catalytic efficiency at the surface of non-planar carbon-based electrocatalytic coatings [9,101–104]. This success has prompted the application of the K–L equation to the assessments of the current study (Table 5). The slope values of the K–L plots (Figs. S7, S9 and S10(B)) are needed to calculate the electron transfer number of the ORR by application of the K–L calculation (Equations S1 and S2) [96,97] (Table 5).

An improvement in the ORR efficiency is most clearly achieved after 4 h of graphite grinding in comparison to the unground or 0.5-hr ground samples. This is apparent from the higher n-number throughout all the applied potentials considered (−0.4 V, −0.6 V and −0.9 V) (Table 5). In another study, vertically aligned carbon nanotubes (VACNT) have shown varied electron transfer efficiency in response to changes in potential, similar to that observed in the current study (n = ~2.2 at −0.4 V; n = ~3.5 at −0.9 V) [105]. Also apparent is the similar electron transfer efficiency of the GP 4-hr sample (n = 1.9 at −0.4 V; n = 3.6 at −0.9 V) to that of the VACNTs produced via thermal chemical vapour deposition. Studies of graphene derived from reduction of graphene oxide have indicated that the high level of oxygen remaining after synthesis causes

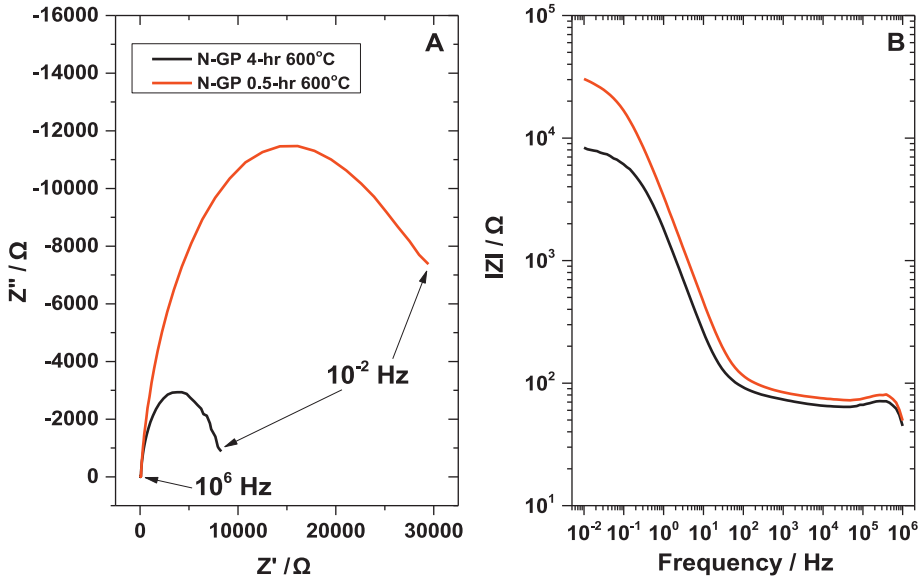

Fig. 10. EIS analysis graphed as a Nyquist plot (A), displaying the real impedance (Z') versus the imaginary impedance (Z''), and a Bode plot (B), illustrating the change in the impedance modulus (IZI) as the frequency (10^6–10^{-2} Hz) of the alternating potential is scanned during analysis of the N-GP 0.5-hr 600 °C and the N-GP 4-hr 600 °C sample. An alternating potential amplitude of 10 mV is applied at a stationary GCE disc (0.0706 cm^{-2}). The N-GP coating is prepared to a density of 0.424 mg cm^{-2}. O_2-saturated 0.1 M KOH electrolyte is used and a potential (−0.1 V) is applied versus an Ag/AgCl reference electrode.

a low electron transfer number [81,106]. A possible reason for the higher ORR efficiency from the GP 4-hr sample (O1s = 3.72 at.%) over that of the graphene presented by Wu et al. (2013) (n = ~2.2 at −0.6 V) is clear when considering the much higher oxygen content (O1s = 23.07 at.%) reported by Wu et al., (2013) [81]. A high oxygen content could inhibit efficient electron transport more so than the composition of the GP 4-hr sample (n = 2.9 at −0.6 V) of the present investigation [107]. For N-GP 4-hr 600 °C sample, the highest kinetic efficiency is indicated by an electron transfer number of 3.8 obtained at −0.9 V. This indicates that the N-GP 4-hr 600 °C sample is close in achieving the high ORR efficiency of a 4-electron transfer at large overpotentials (Table 5), an increase being obtained largely as a result of the incorporation of nitrogen. The beneficial effect of the nitrogen incorporation on the ORR efficiency is highlighted with a lower electron transfer number from the pristine GP samples in comparison to the nitrogen doped counterparts (Table 5).

Another unique material known as graphene-based carbon nitride nanosheets constitute graphene particles between carbon nitride layers [102]. This material provides a n-number of between 2.6 and 4.0 electrons, depending on the temperature applied during production. Optimum electron transfer is facilitated at a pyrolysis temperature of 800 °C (n = 4.0) for the graphene-based carbon nitride, while a further increase in temperature decreases the resultant electron transfer efficiency (n = 3.5) [102]. This is similar to the effect noted in the current study, where optimum ORR catalysis is observed for the N-GP produced at 600 °C, while the sample produced at 700 °C indicates a lower catalytic behaviour (Fig. S16). The hydrothermal reduction of GO to N-graphene, with urea as a source of nitrogen, provided a n-number of 3.0 between −0.4 V and −0.6 V [106], which is inferior to the N-GP 4-hr 600 °C sample of the current study (Table 5).

Other mechanical exfoliation techniques, such as that reported by Jeon et al., (2013), involves milling of graphite in the presence of dopants (hydrogen (n = 3.0), carboxylic acid (n = 2.9) and carboxylic acid/sulfonic acid (n = 2.8)), which provide materials that have a less efficient ORR catalysis than the N-GP 4-hr 600 °C (n = 3.5) and N-GP 0.5-hr 600 °C (n = 3.2) samples of the current investigation [35]. The polarity of the functionalised edges appears to cause the variation in the onset potential for ORR catalysis reported by Jeon et al., (2013) (hydrogen (−0.24 V), carboxylic acid (−0.22 V), carboxylic acid/sulfonic acid (−0.16 V)) [35]. The N-GP samples of the current study provides a more positive onset potential during LSV analysis than the samples reported by Jeon et al., (2013) (N-GP 0.5-hr 600 °C, −0.111 V; N-GP 4-hr 600 °C, −0.081 V). These findings indicate that the facile grinding of graphite in BMIM-PF_6 followed by nitrogen doping can be more favourable than the increasingly popular ball-milling strategies delivering metal-free ORR catalysts. The N-GP samples are similar to some of the N-doped carbon materials of main stream research, but apparent is the opportunity for further enhancement of ORR catalysis in future investigations [8,105,108]. Also noted is the additional manoeuvre required in order to obtain a replica of the ORR catalysis provided by Pt/C (Fig. S17). The purpose of replicating the favourable catalysis of Pt/C is to remove the main obstacle to the omnipresence of fuel cell technology among society, which is the scarcity and high cost of employing precious metal catalysts.

3.7. Methanol tolerance of the N-GP samples

For incorporation of graphite-derived samples as a cathode coating in direct methanol fuel cell (DMFC) devices, a resilient ORR catalysis in the presence of methanol cross over is essential [109,110]. LSV and CV analysis highlight the methanol resistance of the pristine and N-GP samples, allowing an uninhibited ORR current in the presence of 2 M methanol (Figs. S11 and S12; Fig. 11). The methanol resistance of the ORR catalysis facilitated on the N-GP samples is proven to be superior to that of Pt/C in O_2-saturated 0.1 M KOH (Fig. S12; Fig. 11). Fig. S12 and Fig. 11 shows Pt/C providing a significant methanol oxidation at ~−0.09 V in 1 M and

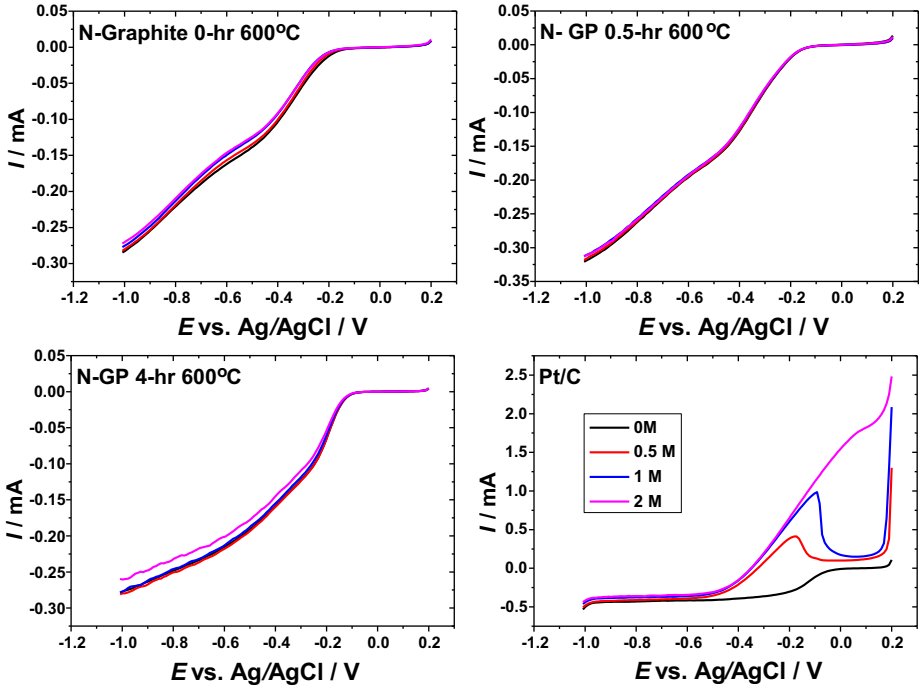

Fig. 11. LSV highlighting the effect of varied methanol concentrations on the current response of the N-GP preparations (0.424 mg cm^{-2} coating) derived from graphite grinding in BMIM-PF_6 for 30 min and 4 h followed by pyrolysis at 600 °C in a 1:10 urea mixing ratio (N-GP 0.5-hr 600 °C; N-GP 4-hr 600 °C). Comparison is made to a 0.424 mg cm^{-2} coating of graphite starting material that was pyrolysed with urea (1:10) at 600 °C (N-graphite 0-hr 600 °C) and a 0.282 mg cm^{-2} coating of platinum on carbon black (Pt/C). Scan rate is 10 mV s^{-1} in O_2-saturated 0.1 M KOH. A glassy carbon electrode disc is used as a working electrode substrate (0.0706 cm^2).

2 M methanol, which assists in the deterioration of ORR onset at the Pt/C catalyst, as these oxidation and reduction reactions occur within a similar potential region [111, 112].

Methanol oxidation at both the cathode and the anode of a DMFC can cause a depolarisation effect, which results in a decrease in the current yield [113]. Figs. S11 and S12 of the supporting information, highlights a similar methanol resistance for the pristine GP and N-GP material coatings during CV analysis, as is observed from LSV evaluations (Fig. S11; Fig. 11).

3.8. ORR current stability in response to varied grinding duration

Chronoamperometry analysis functions in displaying the stability (the ability to recover a decrease of current magnitude during continuous operation [111]) of the electrocatalysts and is a widely accepted method for this determination [42,114–118]. Along with a high ORR activity, a fuel cell catalyst should consistently be capable of producing a stable cathodic current over a significant duration [34,111]. Higher catalytic stability for the pristine GP samples is observed in comparison to Pt/C (Fig. 12). The portion of initial retained current after an 8-h duration is 69.81% for GP 4-hr and 71.48% for the GP 0.5-hr sample. This is significantly more stable than the Pt/C, which retains 60.25% of the initial current detected. Current depletion of the Pt/C can be attributed to degradation of the carbon support, causing crystal migration and subsequent aggregation or detachment of platinum nanoparticles. This decreases the electrochemically active surface area of Pt/C during prolonged analysis [119, 120].

The N-GP 4-hr 600 °C sample exhibits the highest stability of all of the samples analysed with a final retained relative current of 78.89% (Fig. 12). The N-GP 0.5-hr 600 °C sample is similar, but retains a lower portion of the initial current (77.20%). These N-graphene nanoplatelet samples show a superior durability to the pristine GP samples and the Pt/C sample coating (60.25% retention). The Pt/C sample measured in the current study provides a similar current retention behaviour to that of other Pt/C samples assessed [121]. Carbon-based materials doped synergistically with phosphorus and nitrogen display a stability of 85% from chronoamperometry, which is only slightly above that of the present N-GP samples [121]. The current magnitude retained from ORR catalysis at the surface of the N-GP samples is just below that provided by N-graphene produced via plasma treatment, with a final retained current of ~87% of the initial current response [44]. The stability of the N-GP 4-hr 600 °C sample is proven to be similar to that of N-doped carbon samples previously disclosed [7,44]. It is suggested that the abundance of defects in the N-GP samples, as highlighted by Raman spectroscopy data ($I_D/I_G = 0.88$ for N-GP 4-hr 600 °C; $I_D/I_G = 0.86$ for N-GP 0.5-hr 600 °C), has the effect of bestowing a larger degree of cathodic current stability over the pristine GP samples ($I_D/I_G = 0.32$ for graphite 0-hr; $I_D/I_G = 0.76$ for GP 0.5-hr; $I_D/I_G = 0.79$ for GP 4-hr). The carbon lattice defects translating into sites of ORR catalysis.

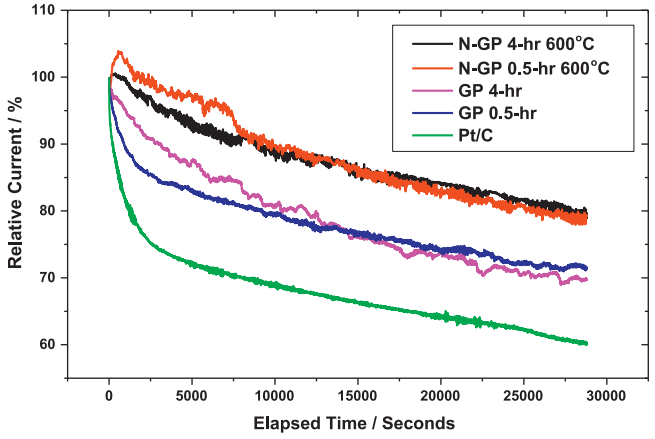

Fig. 12. Stability analysis is calculated from a chronoamperometric response of a 0.424 mg cm^{-2} coating of graphite ground for 30 min (GP 0.5-hr) and 4 h (GP 4-hr), respectively, with subsequent pyrolysis at 600 °C in a 1:10 urea mixing ratio (N-GP 0.5-hr 600 °C; N-GP 4-hr 600 °C). This is compared to a 0.282 mg cm^{-2} particulate coating of Pt/C on a GCE disc (0.0706 cm^{-2}). The potential at which ORR onset occurs for each material was applied throughout the measurement duration in O_2-saturated 0.1 M KOH at a rotation rate of 1600 rpm. Relative current is the detected current displayed as a percentage of the initial current measured at 0 s of elapsed time in the chronoamperometric analysis of each particulate electrode coating.

4. Conclusions

The development of nitrogenated graphene nanoplatelets as a metal-free ORR catalyst in alkaline conditions is reported. The proposed graphite grinding method utilising BMIM-PF_6 offers a possible mass production strategy for pristine and N-doped graphene nanoplatelets in future up-scaled manufacture of fuel cell systems. The highest ORR cathodic current from the developed N-GP samples was from the N-GP 4-hr 600 °C sample, as confirmed during LSV and CV analysis. This sample also promoted a highly efficient electron transfer per reduced oxygen molecule, assisting the provision of an improved cathodic current response. The stability of the ORR current from the pristine GP and N-GP samples is higher than platinum on carbon black, as observed from chronoamperometry. Raman spectroscopy data has confirmed that prolonging the grinding duration promotes an increase in defects upon the carbon lattice of the pristine GP samples and nitrogen incorporation further increases the abundance of defects. As confirmed by XPS, the longer the grinding duration, the higher the incorporation of nitrogen during subsequent pyrolytic treatment. As the nanoplatelet size decreases, the carbon lattice edge plane exposure increases, which allows a higher level of active sites for ORR catalysis. As the edges increase, there are more abundant sites

Table 5
Electrons transferred per reduced molecule of O_2 shown by using the K–L equation. Values are shown for graphite starting material (graphite 0-hr) along with values for graphite ground in BMIM-PF_6 for 30 min (GP 0.5-hr) and 4 h (GP 4-hr), respectively. Accompanying kinetic efficiency data regarding these samples after pyrolysis at 600 °C with a 1:10 ratio of GP or graphite: urea powder mixture is also presented (N-graphite 0-hr 600 °C; N-GP 0.5-hr 600 °C; N-GP 4-hr 600 °C), together with the Pt/C.

Sample name	Material coating density on the GCE disc/mg cm^{-2}	Electron transfer number at −0.4 V	Electron transfer number at −0.6 V	Electron transfer number at −0.9 V
Graphite 0-hr	0.424	1.4	2.1	2.9
GP 0.5-hr	0.424	1.6	2.2	3.3
GP 4-hr	0.424	1.9	2.9	3.6
N-graphite 0-hr 600 °C	0.424	2.2	2.6	3.2
N-GP 0.5-hr 600 °C	0.424	2.7	3.2	3.4
N-GP 4-hr 600 °C	0.424	3.2	3.5	3.8
Pt/C	0.282	4.0	4.2	4.3

for the incorporation of pyrrolic nitrogen and pyridinic nitrogen bonding during pyrolysis in the presence of urea. This further enhances the ORR catalysis after nitrogen doping of the graphene nanoplatelets. More understanding of the pathways taken during incorporation of nitrogen into the carbon lattice is required to enhance design and performance of mass produced graphenic electrode coatings for fuel cell applications.

Acknowledgements

The authors wish to acknowledge the financial support of the Department of Employment and Learning, Northern Ireland, which contributed to the financial requirements during the completion of this study. Appreciation for motivation and helpful support is assigned to Mr. William Hayes, Mrs. Mary Hayes, Mrs. Grace Hayes and Mr. William Bartolome Hayes.

Appendix A. Supplementary data

Supplementary data related to this article can be found at http://dx.doi.org/10.1016/j.jpowsour.2014.06.168.

References

[1] E. Antolini, T. Lopes, E.R. Gonzalez, J. Alloys Compd. 461 (2008) 253–262.
[2] M. Sistiaga, A.R. Pierna, J. Non-Cryst. Solids 329 (2003) 184–187.
[3] K.H. Park, B.H. Kim, S.H. Song, J.K. won, B.S. Kong, Kisuk Kang, S. Jeon, Nano Lett. 12 (2012) 2871–2876.
[4] T. Yamada, M. Ishihara, J. Kim, M. Hasegawa, S. Iijima, Carbon 50 (2012) 2615–2619.
[5] K. Novoselov, A. Geim, S. Morozov, D. Jiang, Y. Zhang, S. Dubonos, I.V. Grigorieva, A.A. Firsov, Science 306 (2004) 666–669.
[6] N. Liu, F. Luo, H. Wu, Y. Liu, C. Zhang, J. Chen, Adv. Funct. Mater. 18 (2008) 1518–1525.
[7] L. Qu, Y. Liu, J.-B. Baek, L. Dai, ACS Nano 4 (2010) 1321–1326.
[8] Z. Wang, R. Jia, J. Zheng, J. Zhao, Li Li, J. Song, Z. Zhu, ACS Nano 5 (2011) 1677–1684.
[9] Z. Yang, H. Nie, X. Chen, X. Chen, S. Huang, J. Power Sources 236 (2013) 238–249.
[10] K.A. Kurak, A.B. Anderson, J. Phys. Chem. C 113 (2009) 6730–6734.
[11] H. Kim, K. Lee, S. Ihl Woo, Y. Jung, Phys. Chem. Chem. Phys. 13 (2011) 17505–17510.
[12] X. Fan, W.T. Zheng, J.-L. Kuo, RSC Adv. 3 (2013) 5498–5505.
[13] S. Maldonado, K.J. Stevenson, J. Phys. Chem. B 109 (2005) 4707–4716.
[14] R.J. Taylor, A.A. Humffray, J. Electroanal. Chem. Interfacial Electrochem. 64 (1975) 85–94.
[15] H. Niwa, K. Horiba, Y. Harada, M. Oshima, T. Ikeda, K. Terakura, J. Ozaki, S. Miyata, J. Power Sources 187 (2009) 93–97.
[16] K.R. Lee, K.U. Lee, J.W. Lee, B.T. Ahn, S.I. Woo, Electrochem. Commun. 12 (2010) 1052–1055.
[17] P.H. Matter, L. Zhang, U.S. Ozkan, J. Catal. 239 (2006) 83–96.
[18] N.P. Subramanian, X. Li, V. Nallathambi, S.P. Kumaraguru, H. Colon-Mercado, G. Wu, J.-W. Lee, B.N. Popov, J. Power Sources 188 (2009) 38–44.
[19] D. Wei, Y. Liu, Y. Wang, H. Zhang, L. Huang, G. Yu, Nano Lett. 9 (2009) 1752–1758.
[20] G. Imamura, K. Saiki, J. Phys. Chem. C 115 (2011) 10000–10005.
[21] X.-J. Li, Chin, J. Chem. Phys. 25 (2012) 325–329.
[22] A. Grüneis, J. Phys. Condens. Matter 25 (2013) 043001.
[23] D. Usachov, O. Vilkov, A. Gruneis, D. Haberer, A. Fedorov, V.K. Adamchuk, A.B. Preobrajenski, P. Dudin, A. Barinov, M. Oehzelt, C. Laubschat, D.V. Vyalikh, Nano Lett. 11 (2011) 5401–5407.
[24] T. Humberto, L. Ruitao, M. Terrones, M.S. Dresselhaus, Rep. Prog. Phys. 75 (2012) 062501.
[25] X.B. Wang, Y.Q. Liu, D.B. Zhu, L. Zhang, H.Z. Ma, N. Yao, B.L. Zhang, J. Phys. Chem. B 106 (2002) 2186–2190.
[26] V. Krstic, G. Rikken, P. Bernier, S. Roth, M. Glerup, Eur. Phys. Lett. 77 (2007) 107–110.
[27] J. Casanovas, J.M. Ricart, J. Rubio, F. Illas, J.M. Jimenez-Mateos, J. Am. Chem. Soc. 118 (1996) 8071–8976.
[28] S. Maldonado, S. Morin, K.J. Stevenson, Carbon 44 (2006) 1429–1437.
[29] J.D. Wiggins-Camacho, K.J. Stevenson, J. Phys. Chem. C 113 (2009) 19082–19090.
[30] T.S. Ong, H. Yang, Carbon 38 (2000) 2077–2085.
[31] N.J. Welham, J.S. Williams, Carbon 36 (1998) 1309–1315.
[32] D. Deng, L. Yu, X. Pan, S. Wang, X. Chen, P. Hu, L. Sun, X. Bao, Chem. Commun. 47 (2011) 10016–10018.
[33] F. Salver-Disma, J. Tarascon, C. Clinard, J. Rouzaud, Carbon 37 (1999) 1941–1959.
[34] E. Antolini, Appl. Catal. B: Environ. 123–124 (2012) 52–68.
[35] I.-Y. Jeon, H.-J. Choi, S.-M. Jung, J.-M. Seo, M.-J. Kim, L. Dai, J.-B. Baek, J. Am. Chem. Soc. 135 (2013) 1386–1393.
[36] D.W. Chang, H.-J. Choi, I.-Y. Jeon, J.-B. Baek, Chem. Rec. 13 (2013) 224–238.
[37] N.G. Shang, P. Papakonstantinou, S. Sharma, G. Lubarsky, M. Li, D.W. McNeill, A.J. Quinn, W. Zhou, R. Blackley, Chem. Commun. 48 (2012) 1877–1879.
[38] X.S. Zhou, T.B. Wu, K.L. Ding, B.J. Hu, M.Q. Hou, B.X. Han, Chem. Commun. 46 (2010) 386–388.
[39] J. Lee, T. Aida, Chem. Commun. 47 (2011) 6757–6762.
[40] M. Tariq, M.G. Freire, B. Saramogo, J.A.P. Coutinho, J.N.C. Lopes, L.P.N. Rebelo, Chem. Soc. Rev. 41 (2012) 829–868.
[41] Y. Xu, Y. Huang, W. Yan, L. Zhang, Y. Chen, J. Nanosci. Nanotechnol. 13 (2013) 1116–1119.
[42] S. Yang, L. Zhi, K. Tang, X. Feng, J. Maier, K. Müllen, Adv. Funct. Mater. 22 (2012) 3634–3640.
[43] S.Y. Yang, Y.L. Chang, Y.L. Huang, Y.F. Lee, H.W. Tien, S.M. Li, Y.H. Lee, C.H. Liu, C.C.M. Ma, C.C. Hu, Electrochem. Commun. 14 (2012) 39–42.
[44] I.-Y. Jeon, D. Yu, S.-Y. Bae, H.-J. Choi, D.W. Chang, L. Dai, J.-B. Baek, Chem. Mater. 23 (2011) 3987–3992.
[45] Y. Si, E.T. Sam, Chem. Mater. 20 (2008) 6792–6797.
[46] C. Liu, G. Hu, H. Gao, J. Supercrit. Fluids 63 (2012) 99–104.
[47] V. Gupta, N. Chaudhary, R. Srivastava, G.D. Sharma, R. Bhardwaj, S. Chand, J. Am. Chem. Soc. 133 (2011) 9960–9963.
[48] S.-S. Kim, J.-Y. Choi, K. Kim, B.-H. Sohn, Nanotechnology 23 (2012) 125301.
[49] XG Sciences, *x*GNP Graphene Nanoplatelets: Grade C, in: About *x*GnP Graphene Nanoplatelets, XG Sciences, Lansing, MI, USA, 2013.
[50] K. Yang, J. He, Z. Su, J.B. Reppert, M.J. Skove, T.M. Tritt, A.M. Rao, Carbon 48 (2010) 756–762.
[51] S.K. Chatterjee, X-ray Diffraction: Its Theory and Applications, second ed., Prentice-Hall of India Pvt. Ltd., New Delhi, 2010.
[52] J. Hao, L. Chen, K. Zheng, Z. Xu, J. Shi, B. Zhou, M. Shan, Y. Li, J. Mater. Sci. 49 (2014) 827–832.
[53] H. Estrade-Szwarckopf, Carbon 42 (2004) 1713–1721.
[54] A. Patterson, Phys. Rev. 56 (1939) 978–982.
[55] P. Scherrer, Nachr. Ges. Wiss. Gött. 2 (1918) 98–100.
[56] A.C. Ferrari, Solid State Commun. 143 (2007) 47–57.
[57] F. Mazzamuto, A. Valentin, C. Chassat, J. Saint-Martin, P. Dollfus, Chin. J. Phys. 49 (2011) 31–40.
[58] A.C. Ferrari, J.C. Meyer, V. Scardaci, C. Casiraghi, M. Lazzeri, F. Mauri, S. Piscanec, D. Jiang, K.S. Novoselov, S. Roth, A.K. Geim, Phys. Rev. Lett. 97 (2006) 187401.
[59] L.M. Malard, M.A. Pimenta, G. Dresselhaus, M.S. Dresselhaus, Phys. Rep. 473 (2009) 51–87.
[60] C. Coleman, R. McIntosh, S. Bhattacharyya, J. Appl. Phys. 114 (2013) 043716.
[61] L. Song, Z. Liu, A. Reddy, N. Narayanan, J. Taha-Tijerina, J. Peng, G. Gao, J. Lou, R. Vajtai, P. Ajayan, Adv. Mater. 24 (2012) 4878–4895.
[62] J.-H. Chen, W.G. Cullen, C. Jang, M.S. Fuhrer, E.D. Williams, Phys. Rev. Lett. 102 (2009) 236805.
[63] Y. Zhang, B. Cao, B. Zhang, X. Qi, C. Pan, Thin Solid Films 520 (2012) 6850–6855.
[64] A. Eckmann, A. Felten, A. Mishchenko, L. Britnell, K. Ralph, K.S. Novoselov, C. Casiraghi, Nano Lett. 12 (2012) 3925–3930.
[65] E.J. Ra, M.-H. Tran, S. Yang, T.H. Kim, C.-S. Yang, Y.J. Chung, Y.K. Lee, I.-J. Kim, H.K. Jeong, Curr. Appl. Phys. 14 (2014) 82–86.
[66] S. Kaciulis, Surf. Interface Anal. 44 (2012) 1155–1161.
[67] Y. Lifshitz, Diam. Relat. Mater. 8 (1999) 1659–1676.
[68] J. Robertson, Diam. Relat. Mater. 14 (2005) 942–948.
[69] D.-Q. Yang, E. Sacher, Langmuir 22 (2006) 860–862.
[70] M. Deifallah, P.F. McMillan, F. Corá, J. Phys. Chem. C 112 (2008) 5447–5453.
[71] S. Maldonado, K.J. Stevenson, J. Phys. Chem. B 108 (2004) 11375–11383.
[72] H.-S. Oh, J.-G. Oh, W.H. Lee, H.-J. Kim, H. Kim, Int. J. Hydrogen Energy 36 (2011) 8181–8186.
[73] L. Lai, J.R. Potts, D. Zhan, L. Wang, C.K. Poh, C. Tang, H. Gong, Z. Shen, J. Lin, R.S. Ruoff, Energy Environ. Sci. 5 (2012) 7936–7942.
[74] H.-H. Yang, R.L. McCreery, J. Electrochem. Soc. 147 (2000) 3420–3428.
[75] C. Song, J. Zhang, in: J. Zhang (Ed.), PEM Fuel Cell Electrocatalysts and Catalyst Layers, Springer, Vancouver, 2008, p. 489.
[76] J. Wu, H. Yang, Acc. Chem. Res. 46 (2013) 1848–1857.
[77] A.G. Pandolfo, A.F. Hollenkamp, J. Power Sources 157 (2006) 11–27.
[78] C.A. Leon y Leon, L.R. Radovic, Marcel Dekker, New York, USA, 1994.
[79] X. Chu, K. Kinoshita, Mater. Sci. Eng. B 49 (1997) 53–60.
[80] R.L. McCreery, Chem. Rev. 108 (2008) 2646–2687.
[81] J. Wu, D. Zhang, Y. Wang, B. Hou, J. Power Sources 227 (2013) 185–190.
[82] A. Gomathi, M.R. Harika, C.N.R. Rao, Mater. Sci. Eng. A 476 (2008) 29.
[83] C.N.R. Rao, A. Nag, Eur. J. Inorg. Chem. 2010 (2010) 4244–4250.
[84] D.J. Belson, A.N. Strachan, Chem. Soc. Rev. 11 (1982) 41–56.
[85] S. Takenaka, M. Kishida, J. Jpn. Pet. Inst. 54 (2011) 80–89.
[86] E.J. Biddinger, U.S. Ozkan, J. Phys. Chem. C 114 (2010) 15306–15314.
[87] S. Wang, D. Yu, L. Dai, D.W. Chang, J.-B. Baek, ACS Nano 5 (2011) 6202–6209.
[88] J. Yan, X. Yuan, W. Yu, W. Lin, W. Ouyang, D. Yuan, H. Meng, F. Xie, J. Power Sources 245 (2013) 772–778.

[89] Z. Mo, R. Zheng, H. Peng, H. Liang, S. Liao, J. Power Sources 245 (2013) 801–807.
[90] T. Hibino, K. Kobayashia, P. Heo, Electrochim. Acta 112 (2013) 82–89.
[91] C.-Z. Guo, C.-G. Chen, Z.-L. Luo, J. Power Sources 245 (2014) 841–845.
[92] L. Zhang, Z. Xia, J. Phys. Chem. C 115 (2011) 11170–11176.
[93] H. Wang, T. Maiyalagan, X. Wang, ACS Catal. 2 (2012) 781–794.
[94] S.-F. Huang, K. Terakura, T. Ozaki, T. Ikeda, M. Boero, M. Oshima, J.-I. Ozaki, S. Miyata, Phys. Rev. B 80 (2009) 235410.
[95] E. Barsoukov, J.R. Macdonald, Impedance Spectroscopy; Theory, Experiment, and Applications, second ed., Wiley Interscience Publications, 2005.
[96] M.-R. Gao, Q. Gao, J. Jiang, C.-H. Cui, W.-T. Yao, S.-H. Yu, Angew. Chem. Int. Ed. 50 (2011) 4905–4908.
[97] S. Treimer, A. Tang, D.C. Johnson, Electroanalysis 14 (2002) 165–171.
[98] J. Koutecky, V.G. Levich, Zh. Fiz. Khim. 32 (1958) 1565–1575.
[99] J. Koutecky, V.G. Levich, Dokl. Akad. Nauk. SSSR 117 (1957) 441–444.
[100] J. Masa, C. Batchelor-McAuley, W. Schuhmann, R.G. Compton, Nano Res. 7 (2014) 71–78.
[101] Z. Yang, Z. Yao, G. Li, G. Fang, H. Nie, Z. Liu, X. Zhou, X. Chen, S. Huang, ACS Nano 6 (2012) 205–211.
[102] S. Yang, X. Feng, X. Wang, K. Müllen, Angew. Chem. Int. Ed. 50 (2011) 5339–5343.
[103] X. Zhou, Z. Yang, H. Nie, Z. Yao, L. Zhang, S. Huang, J. Power Sources 196 (2011) 9970–9974.
[104] Z. Yang, X. Zhou, H. Nie, Z. Yao, S. Huang, ACS Appl. Mater. Interfaces 3 (2011) 2601–2606.
[105] S. Wang , E. Iyyamperumal, A. Roy, Y. Xue, D. Yu, L. Dai, Angew. Chem. Int. Ed. 50 (2011) 11756–11760.
[106] B. Zheng, J. Wang, F.-B. Wang, X.-H. Xia, Electrochem. Commun. 28 (2013) 24–26.
[107] H. Zhao, Z. Peng, W. Wang, X. Chen, J. Fang, J. Xu, J. Power Sources 245 (2014) 529–536.
[108] K. Gong, F. Du, Z. Xia, M. Durstock, L. Dai, Science 323 (2009) 760–763.
[109] R. Liu, D. Wu, X. Feng, K. Müllen, Angew. Chem. Int. Ed. 49 (2010) 2565–2569.
[110] S. Sharma, B.G. Pollet, J. Power Sources 208 (2012) 96–119.
[111] J. Wu, X.Z. Yuan, J.J. Martin, H. Wang, J. Zhang, J. Shen, S. Wu, W. Merida, J. Power Sources 184 (2008) 104–119.
[112] N. Hodnik, M. Bele, A. Recnik, N.Z. Logar, M. Gaberšcek, S. Hocevar, Energy Proc. 29 (2012) 208–215.
[113] A.S. Arico, S. Srinivasan, V. Antonucci, Fuel Cells 1 (2001) 133–161.
[114] Y. Zhang, Y. Gu, S. Lin, J. Wei, Z. Wang, C. Wang, Y. Du, W. Ye, Electrochim. Acta 56 (2011) 8746–8751.
[115] Y. Wang, S. Zhang, H. Chen, H. Li, P. Zhang, Z. Zhang, Electrochem. Commun. 17 (2012) 63–66.
[116] S. Lui, J. Wang, J. Zeng, J. Ou, Z. Li, X. Liu, S. Yang, J. Power Sources 195 (2010) 4628–4633.
[117] H.J. Kim, S.M. Choi, M.H. Seo, S. Green, G.W. Huber, W.B. Kim, Electrochem. Commun. 13 (2011) 890–893.
[118] Y. Hu, P. Wu, Y. Yin, H. Zhang, C. Cai, Appl. Catal. B: Environ. 111–112 (2012) 208–217.
[119] Y. Shao-Horn, W.C. Sheng, S. Chen, P.J. Ferreira, E.F. Holby, D. Morgan, Top. Catal. 46 (2007) 285–305.
[120] X. Yu, S. Ye, J. Power Sources 172 (2007) 133–144.
[121] D. Yu, Y. Xue, Liming Dai, J. Phys. Chem. Lett. 3 (2012) 2863–2870.